Winkler Solution for Seismic Earth Pressures Exerted on Flexible Walls by Vertically Inhomogeneous Soil

Scott J. Brandenberg, M.ASCE[1], Maria Giovanna Durante, M.ASCE[2], George Mylonakis, M.ASCE[3], and Jonathan P. Stewart, F.ASCE[4]

Abstract: A solution for the response of flexible retaining walls excited by vertically propagating shear waves in inhomogeneous elastic soil is obtained using the weak form of the governing differential equation of motion associated with the Winkler representation of earth pressures as a function of relative displacement between the wall and the far field soil. Inputs to the model include the soil shear wave velocity profile, the flexural stiffness of the wall, the elastic boundary conditions at the top and bottom of the wall, the motion at the surface of the retained soil, the distributed mass of the wall, and lumped masses at the top and bottom of the wall. The proposed solution is first verified against an available closed-form Winkler solution for uniform soil, and then with elastodynamic solutions for a wall supporting an infinite uniform elastic soil. A validation exercise is then performed using centrifuge data from flexible underground structures embedded in sand, shaken by suites of ground motions. Seismic earth pressures and bending moments are also computed using limit-equilibrium procedures based on horizontal inertial forces acting within an active wedge. The proposed solution compares favorably with the experimental data, whereas the limit equilibrium procedures produce biased predictions.

[1] Professor and Associate Dean, Department of Civil and Environmental Engineering, 5731 Boelter Hall, University of California, Los Angeles, CA 90095-1593. Email: sjbrandenberg@ucla.edu
[2] Postdoctoral Scholar, Department of Civil, Architectural and Environmental Engineering, University of Texas at Austin, email: mgdurante@utexas.edu
[3] Professor and Chair in Geotechnics and Soil-Structure Interaction, Department of Civil Engineering, University Walk, Clifton BS8, University of Bristol, UK; Adjunct Professor, University of California, Los Angeles, and Khalifa University, UAE. Email: g.mylonakis@bristol.ac.uk.
[4] Professor, Department of Civil and Environmental Engineering, 5731 Boelter Hall, University of California, Los Angeles, CA 90095-1593. Email: jstewart@seas.ucla.edu.

Introduction

Seismic earth pressures on retaining structures have traditionally been computed using three approaches: (1) limit state methods (e.g., the "Mononobe-Okabe" or M-O method and its variants), (2) elastodynamic solutions, or (3) numerical simulations. The M-O method was originally formulated by Okabe (1924) and experimentally verified by Mononobe and Matsuo (1929). This method assumes that a pseudo-static seismic coefficient (k_h) acts upon an active Coulomb-type wedge in frictional soil, which in turn results in an incremental change in the lateral earth pressure coefficient, K_{AE}, over the static active earth pressure coefficient, K_A. Variants on the classical approach derived by means of kinematic limit analysis using non-planar failure surfaces (Chen, 1975; Chen and Liu, 1990), stress fields (Mylonakis et al. 2007), and accounting for the phasing of inertial demands within the retained soil (Steedman and Zeng, 1990) are conceptually alike and provide similar results for the active case. The M-O approach is the standard of practice, and has been incorporated into numerous design documents (e.g., NCHRP 2008 and BSSC 2003).

A problem with the M-O method lies in its inability to account for the fundamental driver of seismic earth pressures, which is relative displacement between the wall and the retained soil in the far field. Nor does the method properly account for the factors that most strongly affect relative displacements, including wall flexibility, frequency content of the ground motion, and soil-structure interaction. Furthermore, it fails to produce a physically meaningful solution when k_h is large enough to cause demand to exceed soil strength on a plane parallel to the surface of the retained soil (e.g., Mylonakis et al. 2007), a condition that is critical in seismically active regions with high design ground motion intensities. Seed and Whitman (S-W) (1970) observed that for levels of k_h up to about 0.4, the M-O solution could reasonably be approximated by $K_{AE} = 0.75k_h$ (a remarkable proportionality between "response" and "excitation" in a purely plastic solution). Because this equation is simple and stable, it is often used in lieu of the M-O method, even when $k_h > 0.4$, which lies beyond the range intended by Seed

and Whitman. For example, Mikola et al. (2016) suggested that the S-W approach produced reasonable predictions of seismic earth pressures acting on fixed-base cantilever walls and cross-braced basement walls in centrifuge tests that produced shaking amplitudes up to about 0.75 g.

Elastodynamic continuum solutions such as those by Wood (1973), Veletsos and Younan (1994a, 1994b), Younan and Veletsos (2000), and Beskos et al. (2015) implicitly account for factors not considered in the M-O method, including excitation frequency, soil stiffness, and in some cases vertical soil inhomogeneity and wall flexibility. These factors all contribute to relative displacement between the wall and free-field soil, and are inherently captured in elastodynamic formulations. To facilitate tractable solutions to the governing equations of motion, boundary conditions typically involve a retained soil layer resting on a rigid base, and the input ground motion is applied at the base of the layer. These solutions tend to produce large earth pressures at the resonant frequencies of the retained soil because of the large soil displacements (relative to the base) that occur at those frequencies. However, for many walls the retained soil rests on materials better represented by a compliant base than a rigid base. As a result, the boundary conditions required to render tractable solutions do not match the boundary conditions present for most walls, and as a result, the strong resonances and associated high earth pressures predicted by most elastodynamic solutions are frequently unrealistic.

Additional limitations of existing elastodynamic continuum solutions include lack of consideration for geometric nonlinearity arising from gapping between the wall and soil, and only indirect accounting for material nonlinearity by selection of strain-compatible modulus and damping values using an equivalent linear approach. Rigorous numerical simulations have the capability to overcome these limitations. Nonlinear soil and structural behavior can be incorporated using appropriate constitutive models; geometric nonlinearity at the soil-wall contact can be included using interface elements, and compliance of the soil beneath the retained soil can be modeled by extending the depth of the domain, or using pertinent wave transmitting boundaries to represent deeper soil layers (e.g., Lysmer and

Kuhlemeyer 1969, Bielak et al. 2003). Nonlinear dynamic numerical simulations are recommended where feasible. However, we recognize that project time/budget constraints often do not permit nonlinear numerical simulations, and special expertise is required.

This paper extends an elastodynamic Winkler solution developed by Brandenberg et al. (2015) that eliminated the rigid base assumption by using the ground motion at the surface of the retained soil as an input rather than the motion at the base of the soil layer. The solution modeled the retaining wall as rigid and massless, and the soil as a uniform elastic continuum. Despite these limiting assumptions, it predicted seismic earth pressure resultants that agreed reasonably well with experimental data and numerical simulations. However, the distribution of seismic earth pressures did not agree well with the experimental data. This paper eliminates the assumption that the wall is rigid and massless, and models the soil as having a vertically inhomogeneous shear wave velocity. The modeling equations are formulated first, and the model is then verified with a number of available closed-form solutions before being partially validated with a suite of experimental data presented by Hushmand et al. (2016).

Problem Statement

The problem considered here consists of flexible wall(s) of height H retaining a soil deposit being excited by vertically propagating shear waves with surface displacement amplitude u_{g0}, as illustrated in Fig. 1. The soil is an elastic continuum with a vertically inhomogeneous shear wave velocity profile $V_s(z)$. Soil-structure interaction is represented by depth-dependent Winkler stiffness intensity $k_y^i(z)$ along the vertical walls, and the walls are constrained by rotational and translational impedance constants at the top and bottom of the wall to represent soil-structure interaction effects above and below the wall, as well as structural components attached to the top and base of the wall that are not explicitly modeled. The walls have constant mass density, ρ_w, Poisson ratio, ν_w, thickness, t_w, Young's modulus, E_w, and plane-strain flexural stiffness, $EI = E_w t_w^3/[12(1-\nu_w^2)]$. Discrete masses m_t and m_b are lumped at the

top and bottom of the wall, respectively, to simulate the inertia of slabs and other elements that are not modeled explicitly. Two configurations are considered: (*i*) an infinite length soil deposit for which the free-field displacement profile is utilized as an input, and (*ii*) a soil deposit of finite length *L* for which the displacement profile at a distance y_{ref} from the wall is utilized as an input. Note that the displacement profile for configuration (*ii*) is influenced by the presence of the walls, and is therefore not "free-field". This condition is utilized to validate the method using experimental data.

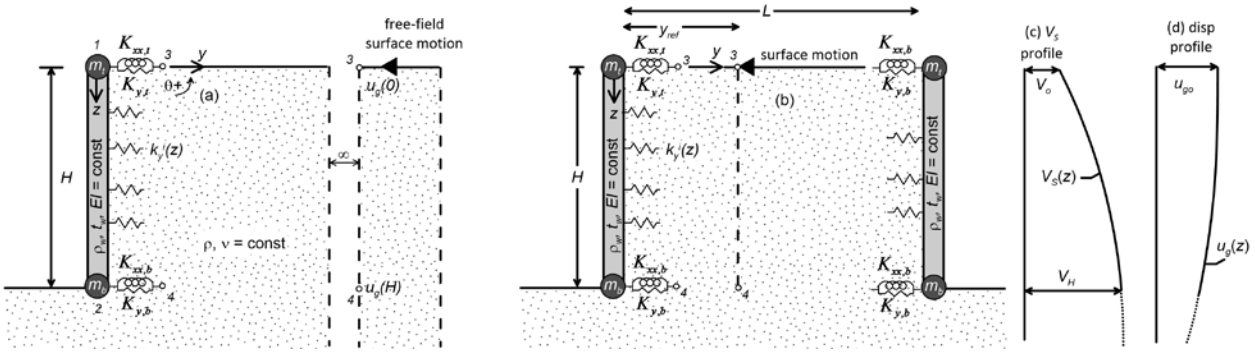

Figure 1. Schematic showing flexible wall(s) retaining (a) an infinite-length soil deposit, and (b) a finite-length soil deposit of (c) vertically inhomogeneous soil being shaken by (d) a ground motion with surface amplitude u_{g0}.

Input Parameters

Shear wave velocity profile

The shear wave velocity profile varies continuously with depth, *z*, following the form by Rovithis et al. (2011) as defined by Eq. 1,

$$V_S(z) = V_H \left[b + (1-b)\frac{z}{H} \right]^n \tag{1}$$

where V_H is the shear wave velocity at the base of the wall, n is a constant that controls the shape of the V_S profile, and b is a constant that controls the ratio of shear wave velocity at the surface, V_o, to that at the base of the wall, $b=(V_o/V_H)^{1/n}$. The shear wave velocity below depth H is not an explicit input parameter to the proposed solution, though it does influence the surface motion due to site response, and also affects the translational and rotational impedance terms at the base of the wall.

Ground motion

The ground surface motion is utilized as an input parameter, which is a departure from many elastodynamic solutions that utilize the ground motion at the base of the deposit, where a rigid boundary is assumed to exist (e.g., Wood 1973, Veletsos and Younan 1994, Kloukinas et al 2012, Beskos et al. 2015). These solutions predict large earth pressures near the natural frequencies of the soil layer resting on the rigid base (e.g., Brandenberg et al. 2015). However, retained soils generally rest on materials more appropriately represented with a compliant base than a rigid one. As a result, solutions derived using a rigid base assumption will produce site responses at resonant frequencies, and associated large earth pressures, that are typically unrealistic. The proposed solution overcomes this issue by utilizing the surface motion as an input parameter rather than the base motion. The surface motion must be selected to be consistent with the site conditions for the problem at hand, which will generally involve analysis of a soil profile that is much deeper than the retained soil. The free-field motion can be obtained from a ground response analysis using a program such as DEEPSOIL (Hashash et al. 2016), or by selecting measured ground motions consistent with seismic hazard for a particular site based on an ergodic site amplification function (e.g., Seyhan and Stewart 2014).

For a given u_{g0} and angular frequency, ω, the depth-dependent displacement profile $u_g(z)$ is solved using the solution developed by Rovithis et al. (2011) as given in Eq. 2,

$$\frac{u_g(z)}{u_{g0}} = \frac{\pi}{2}\sqrt{b}sp^{\frac{1-2n}{2}}\left[J_{\alpha+1}\left(b^{1-n}s\right)N_{\alpha}\left(sp^{1-n}\right) - J_{\alpha}\left(sp^{1-n}\right)N_{\alpha+1}\left(b^{1-n}s\right)\right] \quad (2)$$

where $s = a_o \Big/ \left[\left(1-b\right)\left(1-n\right)\right]$, $p = b + \left(1-b\right)\frac{z}{H}$, $a_o = \omega H/V_H$ is a dimensionless frequency, and J_α and N_α are Bessel functions of the first and second kind, respectively, of order $\alpha = (2n-1)/(2-2n)$.

Winkler stiffness intensity

The Winkler stiffness intensity, $k_y^i\left(z\right)$, is a function of depth, as defined by Eq. 3, where k_{yH}^i is the Winkler stiffness intensity at the base of the wall, and $f(z)$ is a function that defines the variation of Winkler stiffness intensity with depth. The function $f(z)$ is the same as the form of the variation of shear wave velocity with depth, except that the exponent $2n$ is introduced to account for the fact that shear modulus is proportional to V_s^2. The value of k_{yH}^i is computed using Eq. 4, where k_{yHo}^i is the static Winkler stiffness intensity at the base of the wall based on the solution by Brandenberg et al. (2017), as defined by Eq. 5, and ζ_{freq}, ζ_{flex}, and ζ_{length} are scalar adjustment factors to account for frequency, wall flexibility, and finite deposit length respectively.

$$k_y^i(z) = k_{yH}^i \cdot f\left(z\right) = k_{yH}^i \cdot \left[b + \left(1-b\right)\frac{z}{H}\right]^{2n} \quad (3)$$

where,

$$k_{yH}^i = k_{yHo}^i \cdot \zeta_{freq} \cdot \zeta_{flex} \cdot \zeta_{length} \quad (4)$$

in which,

$$k_{yHo}^i = \frac{G_H}{H}\frac{2}{\sqrt{\left(1-\nu\right)\left(2-\nu\right)}}\left[1.06 \cdot e^{-1.97(1-2n)-3.01b} + \frac{\pi}{2}\right] \quad (5)$$

Scaling term ζ_{freq} captures the influence of wave propagation through the retained soil on the Winkler stiffness intensity, as defined by Eq. 6 (Kloukinas et al. 2012),

$$\zeta_{freq} = \sqrt{1 - \frac{a_o^2}{\hat{a}_{oc}^2}} \tag{6}$$

where $\hat{a}_{oc}$ is the first-mode dimensionless natural frequency for the portion of the soil deposit above the base of the wall, which potentially may be of finite length. For the case of an infinitely long soil deposit behind the wall, $\hat{a}_{oc} = a_{oc}$, which is given by Eq. 7 (Brandenberg et al. 2017),

$$a_{oc} \approx \frac{\pi}{2} - 0.406 \cdot e^{-1.95(1-2n)-2.11b} \tag{7}$$

A more general solution for backfills of finite length *L* is given by the theoretical expression in Eq. 8,

$$\hat{a}_{oc}^{\ 2} \approx \frac{\frac{2}{1-\nu}\frac{a_{oc}}{b_{oc}\psi_e}\left[\sinh\left(\frac{L}{H}\frac{a_{oc}b_{oc}}{\psi_e}\right) - \frac{L}{H}\frac{a_{oc}b_{oc}}{\psi_e}\right]}{2\frac{L}{H} - \frac{3\psi_e}{a_{oc}b_{oc}}\sinh\left(\frac{L}{H}\frac{a_{oc}b_{oc}}{\psi_e}\right) + \frac{L}{H}\cosh\left(\frac{L}{H}\frac{a_{oc}b_{oc}}{\psi_e}\right)} + a_{oc}^{\ 2} \tag{8}$$

where $\psi_e^2 = (2\text{-}\nu)/(1\text{-}\nu)$ is a compressibility coefficient and b_{oc} is a stiffness multiplier accounting for the heterogeneity of the soil deposit (Eq. 9). For finite-length deposits, $\hat{a}_{oc} > a_{oc}$ due to the confining effect provided by the two walls. Note that $\hat{a}_{oc} = a_{oc}$ when L = ∞.

$$b_{oc} \approx 1 + 1.17 \cdot e^{-2.16(1-2n)-2.97b} \tag{9}$$

Scaling term ζ_{flex} is required because Winkler stiffness intensity is higher for flexible walls than for rigid walls due to mobilization of shear stresses at the soil-wall interface caused by wall rotation during flexure. Continuum finite element solutions were used to develop an approximate solution for ζ_{flex} (Eq. 10) that depends on a dimensionless Winkler constant β_o given by Eq. 11 (modified from Durante et al. 2018).

$$\zeta_{flex} = 1 + exp\left[1.28 + \frac{0.95 \cdot b - 1.56 \cdot n - 4.87}{(\beta_0 H)^{0.80}}\right] \tag{10}$$

$$\beta_o = \sqrt[4]{\frac{k_{yHo}^i}{4EI}} \tag{11}$$

Scaling term ζ_{length} was derived from the solution by Brandenberg et al. (2017) for two rigid walls retaining a finite-length inhomogeneous elastic soil deposit, and is given by Eq. 12. The value of ξ_{Length} is larger than unity because (i) the two walls provide a stiffening effect that increases Winkler stiffness intensity, and (ii) the displacement profile at y_{ref} is smaller than in the "free-field" due to the restraining effects of the walls. For a given pressure at the soil-wall interface, the Winkler stiffness intensity must therefore be higher for a reference displacement profile at y_{ref} compared with a free-field reference displacement profile. The expression in Eq. (11) goes to unity when free-field conditions are allowed to occur in the retained soil (i.e., $y_{ref} \to \infty$ and $L \to \infty$). Wall flexibility likely influences the effect of deposit length on Winkler stiffness intensity, but that effect has not yet been systematically quantified.

$$\zeta_{length} = \frac{1-\exp\left(-\frac{b_{oc}\sqrt{\hat{a}_{oc}^{\,2}-a_o^{\,2}}}{\psi_e}\frac{L}{H}\right)}{1-\exp\left(-\frac{b_{oc}\sqrt{\hat{a}_{oc}^{\,2}-a_o^{\,2}}}{\psi_e}\frac{y_{ref}}{H}\right)+\exp\left(-\frac{b_{oc}\sqrt{\hat{a}_{oc}^{\,2}-a_o^{\,2}}}{\psi_e}\frac{L}{H}\right)-\exp\left(-\frac{b_{oc}\sqrt{\hat{a}_{oc}^{\,2}-a_o^{\,2}}}{\psi_e}\frac{L-y_{ref}}{H}\right)} \tag{12}$$

Wall Boundary Conditions

The wall is represented as an elastic Euler-Bernoulli plate with constant flexural stiffness, *EI*, constrained by horizontal and rotational springs at the top and bottom of the wall (Fig. 1). Stiffness constants at the top and base of the wall arise from two different contributions: (i) from the soil below the base and/or above the roof diaphragm, and (ii) from structural components connected to the roof and/or base diaphragms. The equations for the springs employ a notation in which $\widehat{K}$ denotes the contribution from the soil, $\widetilde{K}$ denotes the contribution from structural components connected to the top and/or bottom of the wall, subscript "*y*" denotes horizontal translational stiffness, "*xx*" denotes rotational stiffness, "*t*" denotes the top of the wall, and "*b*" denotes the base of the wall.

The $\widehat{K}$ terms produce reactions as a result of relative displacement between the wall and the soil either in the free-field for infinite length deposits, or at location y_{ref} for finite-length deposits. Soil

displacements at the top and base of the wall are $u_g(0)$, and $u_g(H)$, respectively, while soil rotations are zero for vertically propagating shear waves. Assuming a footing of width 2*B* supports the wall, and the depth from the bottom of the wall to a rigid layer is *D*, solutions for $\widehat{K}_{y,b}$ and $\widehat{K}_{xx,b}$ for rigid footings resting on uniform elastic soil are given in Eqs. 13 and 14 (modified from Gazetas and Roesset, 1976; Katsiveli 2020),

$$\widehat{K}_{y,b} = \frac{2.1\overline{G_b}}{2-\nu}\left[1+3\nu\left(2-\nu\right)\frac{B}{D}\right] \tag{13}$$

$$\widehat{K}_{xx,b} = \frac{\pi\overline{G_b}B^2}{2\left(1-\nu\right)}\left(1+\frac{1}{5}\frac{B}{D}\right) \tag{14}$$

where $\overline{G_b}$ is the average shear modulus over the depth interval from *H* to min(*H*+*B*, H+*D*), and is computed from the time-averaged shear wave velocity over this depth interval. Values of $\widehat{K}_{xx,t}$ and $\widehat{K}_{xx,t}$ are zero for the applications presented herein because the top of the wall is flush with the ground surface. However, these terms would be non-zero for structures whose top is embedded beneath the ground surface, and are therefore included in the formulation so that it is extensible to more deeply embedded structures. For cases with flexible diaphragms, an equivalent Winkler method is used to compute the flexural stiffness terms, as presented in the Appendix.

Governing Differential Equation

The governing differential equation for the wall is given by Eq. 15, where $\frac{\partial^2 u(z)}{\partial t^2} = -\omega^2 u(z)$ for a harmonic motion:

$$EI\cdot\frac{\partial^4 u(z)}{\partial z^4} - k_{yH}^{i}\ f(z)\left[u_g(z)-u(z)\right] - \omega^2\rho_w t_w u(z) = 0 \tag{15}$$

A weak form approximation is adopted here to develop an analytical solution. The u_g term is first moved to the right side of the expression, and both sides are multiplied by a set of depth-dependent shape functions, $\Phi_j(z)$, and then integrated over the wall height (Eq. 16).

$$EI\int_0^H \frac{\partial^4 u(z)}{\partial z^4}\Phi_j\, dz + k_{yH}^i \int_0^H f(z)u(z)\Phi_j(z)\,dz - \rho_w t_w \omega^2 \int_0^H u(z)\Phi_j(z)\,dz = k_{yH}^i \int_0^H f(z)u_g(z)\Phi_j(z)\,dz \quad (16)$$

A trial displacement, $\hat{u}$, is defined as the sum of shape functions multiplied by coefficients, c_i (Eq. 17).

$$\hat{u} = \sum_i c_i \Phi_i \quad (17)$$

The solution is exact if the shape functions match the actual displaced shape of the wall, but such shape functions generally cannot be obtained. We apply Hermite cubic polynomial shape functions (Eq. 18) to approximate the displaced shape of the wall. These functions are traditionally utilized to develop stiffness matrix solutions for a Bernoulli-Euler plate (McGuire et al. 2015), and are a reasonable approximation for beams that are stiff relative to the soil, as illustrated later.

$$\Phi_i = \begin{Bmatrix} \left(1-\frac{z}{H}\right)^2\left(1+2\frac{z}{H}\right) \\ z\left(1-\frac{z}{H}\right)^2 \\ \left(\frac{z}{H}\right)^2\left(3-2\frac{z}{H}\right) \\ -\frac{z}{H}^2\left(1-\frac{z}{H}\right) \end{Bmatrix} \quad (18)$$

The c_i coefficients are computed as described in the Appendix, and the coefficients are substituted into Eq. 17 to obtain an approximate displacement function. Although this function may provide a reasonable approximation to the true displacements, it should not be differentiated to compute accurate profiles of bending moment, shear, and subgrade reaction (e.g., Scott 1981). In fact, the subgrade reaction is proportional to the fourth derivative of wall displacement, which is zero since

Hermite cubic polynomials were used, which clearly illustrates that the derivatives of the test displacement functions are inaccurate. Rather, subgrade reaction is computed by equilibrium considerations using Eq. 19, and subsequently post-processed to obtain shear and bending moment diagrams. The subgrade reaction expression in Eq. 19 is divided into two components; the earth pressure component is the Winkler stiffness intensity multiplied by the relative displacement, and includes earth pressures arising from kinematic and inertial interaction effects. The wall inertia component captures the contribution to bending moment of the distributed mass along the wall height, which acts in addition to the earth pressure component. The wall inertia component can be conceptualized as the equivalent pressure that would have to be applied to a massless wall to generate the bending moment profile produced by the distributed inertial forces acting along the wall height. The wall inertia component is therefore not an externally applied pressure acting at the soil-wall interface, but rather an equivalent pressure (i.e., a body force) that accounts for the influence of wall inertia on bending moment. Values of shear and bending moment at the top and base of the wall are computed from the known nodal displacements and the stiffness boundary conditions at the top and bottom of the wall, and provide the necessary boundary conditions for numerical integration of Eq. 19 by the trapezoidal rule to obtain shear and bending moment distributions along the wall height.

$$\underbrace{EI \cdot \frac{\partial^4 u(z)}{\partial z^4}}_{\substack{\text{Change in shear} \\ \text{force with depth}}} = \underbrace{k_{yH}^{i}\ f(z)\left[u_g(z) - u(z)\right]}_{\text{Earth Pressure, } \Delta\sigma} + \underbrace{\rho_w t_w \omega^2 u(z)}_{\text{Wall Inertia}} \tag{19}$$

Single Frequency and Frequency Domain Solutions

The modeling equations formulated herein can be implemented using two approaches: a single frequency approach, or a frequency domain approach. In the single frequency (i.e., monochromatic) approach, a representative value of u_{g0} and ω are selected to model a specific ground motion. These two

input parameters can accurately represent a harmonic motion, but additional research is needed to clarify selection of representative values of u_{g0} and ω for a broadband ground motion. We restrict our use of the single frequency solution to comparisons with analytical solutions in this paper, while we use the frequency domain solution to compare with experimental observations arising from broadband ground motions.

The frequency domain solution utilizes a surface motion time series as an input, and synthesizes contributions of all frequencies in the input motion. Steps implemented in the frequency domain solution are (see also Brandenberg et al. 2015):

(1) compute the Fourier transform of the surface motion, Fu_{g0}.

(2) for each component of Fu_{g0} compute stiffness and mass matrices and force vectors and solve for {c} by inverting Eq. 25 (note there is a separate $\mathbf{c}$ for each frequency component).

(3) for each $\mathbf{c}$ compute reaction forces as

$$\mathbf{F}^{\mathbf{reac}} = \left[\mathbf{K}^{\mathbf{a}} + \mathbf{K}^{\mathbf{b}} - \mathbf{M}^{\mathbf{a}}\right]\mathbf{c} - \mathbf{F}^{\mathbf{a}} \tag{20}$$

where $\mathbf{F}^{\mathbf{reac}}$ is a vector consisting of the Fourier coefficients of the shear and bending moment at the top and bottom of the wall. The stiffness matrices and force vectors in Eq. (20) are derived in the Appendix.

(4) compute the inverse Fourier transform of each component of $\mathbf{F}^{\mathbf{reac}}$ to obtain shear and moment time series at the top and bottom of the wall.

(5) at the time of the peak bending moment, compute the soil and wall displacement at N points evenly distributed along the height of the wall using Eqs. 2 and 17, respectively (N=10 was used for the solutions presented herein).

(6) compute the components of earth pressure at each of the *N* points along the wall using Eq. 19.

(7) using the known shear and bending moment at the top of the wall as boundary conditions, use the trapezoidal rule to integrate the pressures from (6) to obtain values of shear and bending moment at the N points along the wall.

To facilitate implementation of the proposed solution, Jupyter notebooks and files necessary to run the notebooks have been published in the DesignSafe cyberinfrastructure (Brandenberg and Durante 2019). Published data products include a Python script called "SeismicEarthPressure.py" that contains functions that implement the proposed solution, two Jupyter notebooks "FrequencyDomainExamples.ipynb" and "SingleFrequencyExamples.ipynb" that import the Python script as a library and compute solutions for various combinations of soil conditions and wall flexibility conditions, a ground motion file from the Pacific Earthquake Engineering NGA-West2 database "RSN1077_NORTHR_STM-090.DT2", which is the 090 component of the displacement record from the Santa Monica City Hall during the 1994 Northridge earthquake, and an image file "Schematic.png" that defines the inputs to the models. Our intention in publishing these files is to make the calculations easily accessible to anyone interested in using them.

Verification Against Published Solutions

In this section we compare the proposed solution with other solutions from the literature to verify its suitability to evaluate seismic earth pressures, albeit for idealized conditions. The first verification is against a closed-form exact Winkler solution for uniform elastic soil and a massless wall (inspired by a solution available for piles by Anoyatis et al. 2013). The second is against an elastodynamic solution presented by Younan and Veletsos (2000).

Closed-Form Exact Winkler Solution

This section compares the proposed solution with a closed-form exact Winkler solution for uniform elastic soil and a massless wall. By comparing with an exact Winkler solution, we are able to assess the errors introduced by the weak formulation and the use of Hermite cubic polynomial shape functions. For a uniform elastic soil profile, $f(z) = 1$ and $u_g(z) = \cos(kz)$, where $k = \pi/2H$ was selected to model a condition in which the free-field soil displacement is zero at the base of the wall. The uniform elastic solution is given by Eq. 21 (e.g., Anoyatis et al. 2013).

$$u(z) = \chi_1 e^{\beta_o z}\cos(\beta_o z) + \chi_2 e^{\beta_o z}\sin(\beta_o z) + \chi_3 e^{-\beta_o z}\cos(\beta_o z) + \chi_4 e^{-\beta_o z}\sin(\beta_o z) + \frac{k_{yi}u_{g0}\cos(kz)}{EI\cdot k^4 + k_{yi}} \quad (21)$$

The beam was free against translation and rotation at the top and fixed to the soil at the base (i.e., K_{yb} = $K_{xxb} = \infty$, $K_{yt} = K_{xxt} = 0$), and the χ factors were solved to enforce these boundary conditions.

Figure 2 shows distributions of wall and soil displacement, seismic pressure increment, shear force, and bending moment, where all quantities have been presented in dimensionless form. The solutions are presented for values of $\beta_o H$ = 0.5, 1.0, 1.5, and 2.0, where the smaller values correspond to a stiffer wall relative to the soil. The errors in the solution are negligible for $\beta_o H$ = 0.5 and 1.0 for all of the plotted data quantities, and very small for $\beta_o H$ = 1.5 and 2.0. Most reinforced concrete cantilever retaining walls must be stiff enough to limit static deformations to reasonable amounts, and generally have $\beta_o H$ = 1 to 2. Furthermore, the errors are most visible in the plots of displacement and seismic pressure increment, and less significant for shear and bending moment. Bending moment is considered the most important response metric for design purposes. In general, the proposed approximate solution produces excellent agreement with the closed-form solution.

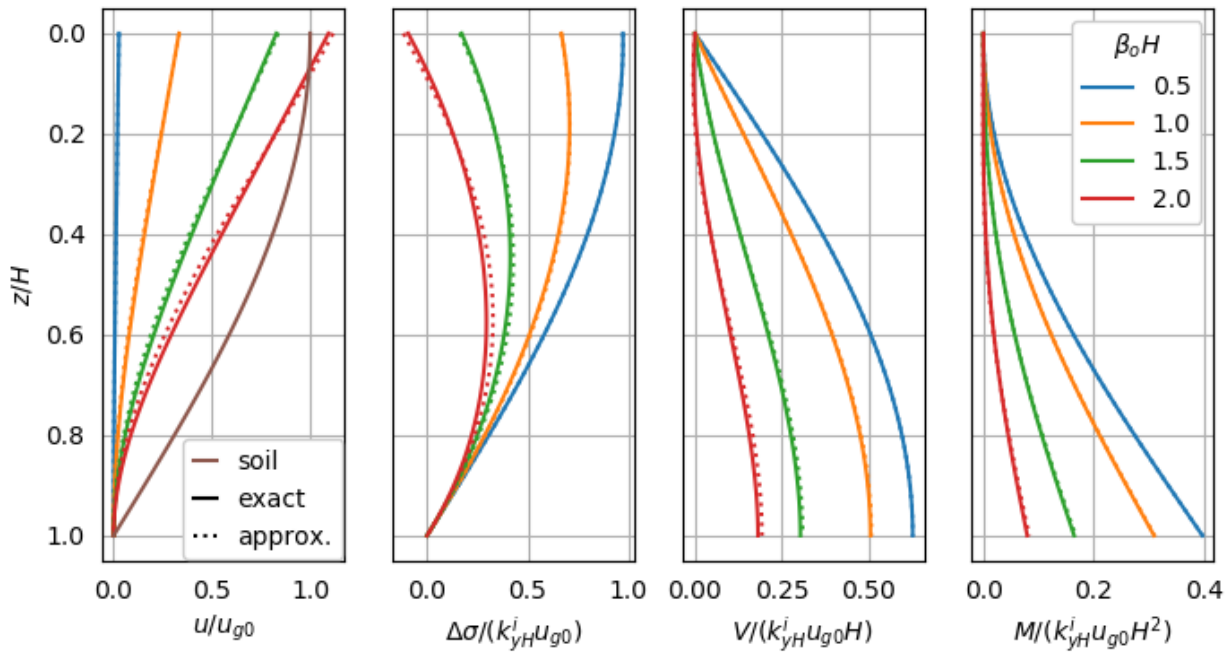

282

283 **Figure 2.** Distributions of dimensionless quantities including (a) wall and soil displacement, (b) seismic

284 pressure increment, (c) shear force, and (d) bending moment.

285 Comparison to Elastodynamic Solution

286 Younan and Veletsos (2000) developed solutions for the dynamic response of flexible retaining walls

287 supporting an infinitely long deposit of uniform elastic soil. We compare predictions of the model

288 proposed herein with their solutions for flexible walls. Seismic demands are applied in the form of a

289 horizontal static body force (corresponding to $\omega = 0$) imposed on the soil deposit. A few definitions are

290 required to relate their results to those formulated here. First, their solutions are formulated in terms of

291 a dimensionless stiffness parameter, d_w, that is related to $\beta_o H$ as indicated in Eq. 22,

$$d_w = (\beta_o H)^4 \frac{8(1-\nu_w^2)}{\pi \cdot \psi_\sigma} \tag{22}$$

292 where $\psi_\sigma = 2/\sqrt{(1-\nu)(2-\nu)}$ and ν_w is the Poisson ratio for the wall material. Younan and Veletsos

293 (2000) utilized $\nu = 1/3$ and $\nu_w = 0.17$ in their solutions, and the same parameters are adopted here.

Second, their solutions utilize the horizontal acceleration at the bottom of the retained soil, $\ddot{u}_{gH}$, as a normalizing factor, whereas we utilize the free-field displacement at the ground surface. Furthermore, our solution requires an input frequency larger than 0, and therefore does not strictly apply to problems with uniform horizontal acceleration. To overcome these issues, we utilize a long wavelength in our solution, $\lambda/H = 200$, corresponding to $kH = \pi/100$. The relationship between acceleration and surface displacement is given by Eq. 23.

$$u_{g0} = \frac{\rho H^2 \ddot{u}_{gH}}{2G\left[1-\cos\left(kH\right)\right]} \tag{23}$$

A comparison of the solutions is provided in Fig. 3. The pressure distributions in Fig. 3a exhibit the same general trends in which wall flexibility reduces earth pressures overall. However, the distributions for the proposed solution tend to have a smaller resultant force, P_E, with a higher line of action, h/H, where h is the distance to the resultant from the base of the wall. This trend is consistent with the finding of Veletsos and Younan (1994) that analyses involving only the fundamental mode of soil and wall deformation predict a higher h/H than analyses involving all modes. The solution for k^i_{yH} in Eq. (3) utilizes shape functions for the soil deformation profile that correspond to the first mode. Although the proposed solution over-predicts h/H and under-predicts P_E, the combined effect provides bending moment values that agree well with the solution by Younan and Veletsos. The reasonable agreement is encouraging because the proposed solution is significantly simpler to implement than the series solution by Younan and Veletsos (2000), and is easily extensible to vertically inhomogeneous soil. Furthermore, continuum elastic solutions, such as those implemented by Younan and Veletsos, exhibit a singularity at the top of flexible walls in which the horizontal pressure asymptotically approaches -∞ (e.g., Borowicka 1939). This singularity is unrealistic for real soils, and does not occur in the Winkler approximation.

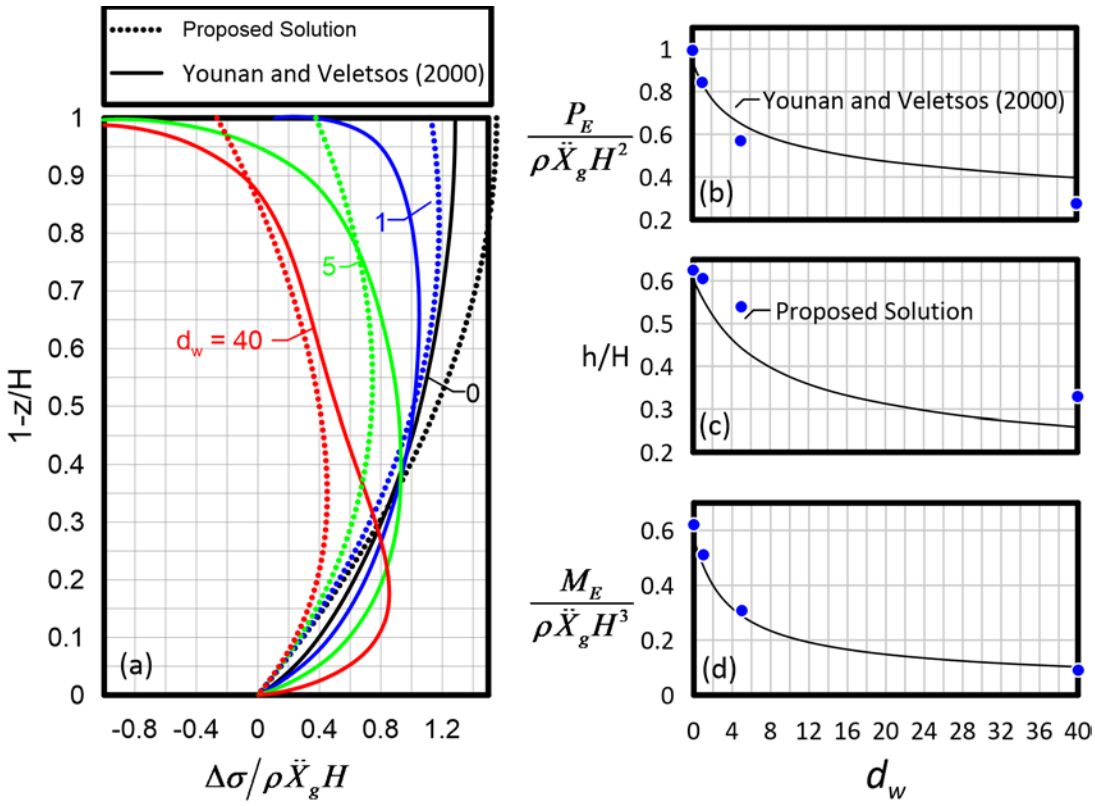

314

315 **Figure 3.** Comparison of proposed solution with Younan and Veletsos (2000) showing (a) pressure
316 distributions, (b) dimensionless soil thrust, (c) dimensionless line of action of resultant, and (d)
317 dimensionless overturning moment.

318 **Validation Against Experimental Data**

319 Model-To-Data Comparisons

320 The proposed solution is compared with measurements from an experimental program by
321 Hushmand et al. (2016) involving steel box structures embedded in sand as illustrated in Fig. 4. Testing
322 was performed on the 5.5 m-radius, 400g-ton geotechnical centrifuge at the University of Colorado
323 Boulder. Comparisons are made for three tests, with model properties summarized in Table 1. For Test
324 2, the structure was bolted to the base of the container, whereas for Tests 1, and 4, the structures were
325 resting on sand as illustrated in Fig. 4. Test 3 is not used here because the tactile pressure sensors did

not function properly during the test. Dry Nevada sand No. 120 (G_s = 2.65, e_{min} = 0.56, e_{max} = 0.84, D_{50} = 0.13mm, C_u = 1.67, ρ = 1.6Mg/m^3) was placed at a relative density of D_r = 60%. The structures were composed of steel with ρ = 7.87 Mg/m^3 and E = 200 GPa. Assuming that the shear beam container provides harmonic boundary conditions (*i.e.*, equivalent to an infinite sequence of identical models connected to each other in series from left-to-right), the centrifuge model represents a finite length deposit with the length of the retained soil deposit equal to twice the distance from the container wall to the structure wall, such that L = 30 m. Furthermore, the accelerometer that recorded the surface input motion was positioned at a distance from the wall of the structure of y_{ref} = 11m. The structural response was measured using strain gauges mounted on the structure walls, and tactile pressure sensors placed at the interface between the sand and the structure walls.

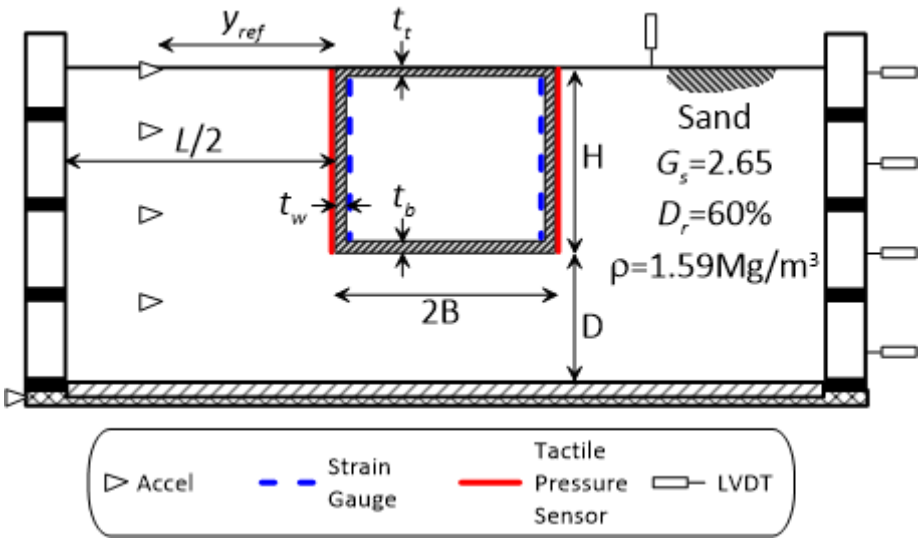

Figure 4. Experimental configuration scheme (modified after Hushmand et al. 2016).

Table 1. Properties of centrifuge models at prototype scale (Hushmand et al. 2016).

Test ID	*H* (m)	*B* (m)	*D* (m)	*L* (m)	y_{ref} (m)	t_w (m)	t_t (m)	t_b (m)	V_H (m/s)	$K_{y,t}$ (kN/m/m)	$K_{xx,t}$ (kN-m/rad/m)	$K_{y,b}$ (kN/m/m)	$K_{xx,b}$ (kN-m/rad/m)
Test 1	10.5	6.1	8.3	30	11	0.56	0.37	0.69	186	0	8.7e5	1.7e5	6.0e6
Test 2	10.5	6.1	0	30	11	0.56	0.37	0.69	186	0	8.7e5	∞	∞
Test 4	10.5	6.1	8.3	30	11	0.28	0.28	0.50	186	0	3.7e5	1.7e5	2.5e6

Shear wave velocity was not directly measured in the experiments, but rather inferred from ambient vibration data. Hushmand et al. (2016) reports that the natural frequency of the soil deposit was 4.0 Hz for Test 2. Assuming n = 0.25, b = 0.01, and ν = 0.3, which are reasonable values for cohesionless sand, the dimensionless natural frequency computed using Eq. 7 is a_{oc} = 1.42. The value of shear wave velocity at the elevation of the base of the wall is then computed as V_H = 186 m/s using Eq. 24. The sand was prepared in the same manner for all of the tests, so the same value of V_H was used for Tests 1 and 4.

$$V_H = \frac{2\pi f_o H}{a_{oc}}\left[b+(1-b)\right]^{-n} \tag{24}$$

Time-averaged values of V_S were then computed over the depth range from H to H+D for Tests 1 and 4, and values of base stiffness $\widehat{K}_{y,b}$ and $\widehat{K}_{xx,b}$ were computed using Eqs. 13 and 14. These values were then divided by two to account for the fact that two walls were attached to the same base slab. The rotational stiffness at the top of the wall was computed from the flexural stiffness of the roof diaphragm as $\widetilde{K}_{xx,t} = 6EI / B$ and the translational stiffness at the top of the wall was $\widetilde{K}_{y,t} = 0$ since there were no columns or interior walls connecting the roof and floor diaphragms.

A sequence of earthquake ground motions was imposed on the model using the servo-controlled, electro-hydraulic shake table. The motions consisted of the following scaled horizontal records: Sylmar Converter Station component NCS52 from the 1994 Northridge Earthquake, the LGPC Station component LGP000 from the 1989 Loma Prieta Earthquake, and the Istanbul Station component IST180 from the 1999 Izmit Earthquake in Turkey. Hushmand et al. (2016) adopted a naming convention in which the motions were assigned names based on the earthquake from which they were recorded (i.e., Izmit, Loma Prieta, and Northridge), and this naming convention is utilized here for consistency with the source manuscript. Three intensities were used for the Northridge motion, and are denoted Northridge-

363 L (low intensity), Northridge-M (medium intensity), and Northridge-H (high intensity). We obtained
364 recorded motions from the surface of the model from Dashti (personal communication, 2017). We
365 band-pass filtered the records using an acausal Butterworth filter with high-pass corner frequency and
366 order of 0.2Hz and 2, respectively, and low-pass corner frequency and order of 6.0Hz and 5,
367 respectively. High pass filtering was required to remove low frequency noise to obtain accurate velocity
368 and displacement time series. The motions were also low-pass filtered to remove low-amplitude and
369 high-frequency portions of the records, which were observed to cause undesired resonances in the
370 computed solutions for some motions.

371 Softening of the models due to strong shaking was observed in the form of lengthening of the
372 fundamental period of the soil column, therefore an equivalent linear approach was implemented for
373 the model predictions. Hushmand et al. (2016) adopted a modulus reduction relationship by Darendeli
374 (2001) for the sand, and the same modulus reduction curve is adopted herein. The average shear strain
375 in the soil over the height of the wall was obtained by taking the difference in displacement at the
376 ground surface, and the displacement computed at the base of the wall using Eq. 2. Embedded
377 accelerometers could conceivably be used to obtain more accurate shear strain estimates, but we did
378 not use these sensors because we wanted our predictions to be consistent with the modeling
379 assumption in which only the surface motion, soil properties, and structural properties are known. A
380 strain-compatible shear wave velocity, $V_{H,eq}$, was obtained by the following steps: (1) assume a value of
381 $V_{H,eq}$, (2) compute the soil displacement time series at the elevation of the top of the wall and of the
382 bottom of the wall (Eq 2), (3) compute a time series of average strain over the wall height as the
383 difference in displacements divided by wall height, and find the maximum value, γ_{max}, (4) compute a
384 representative shear strain, $\gamma_{eff} = \gamma_{max}$ (M_w-1)/10 following Idriss and Sun (1996), where M_w is the
385 moment magnitude for the earthquake from which the ground motion record was obtained, (5) obtain a

386 G/G_{max} value from the modulus reduction curve, and compute $V_{H,eq} = V_H(G/G_{max})^{0.5}$, and (6) repeat steps
387 2 through 5 until the computed value of γ_{eff} is consistent with $V_{H,eq}$.

388 Predicted profiles of wall displacement, seismic earth pressure component $\Delta\sigma_k$, and bending
389 moment *M* are presented in Fig. 5 for Test 2 with the Northridge-L motion, and in Fig. 6 for Test 1 with
390 the Loma Prieta motion. The measured peak horizontal pressure and bending moment profiles are also
391 plotted. The tactile pressure sensors and strain gauges were connected to different data acquisition
392 systems that were not synchronized. Therefore, the measured pressure data are plotted at the time that
393 the peak pressure was measured rather than at the time the peak bending moment was measured. The
394 tactile pressure transducers directly measure the pressure at the soil-wall interface, and are compared
395 in Figs. 5-6 with predicted values of $\Delta\sigma$, which represents earth pressures at the soil-wall interface. The
396 predicted interface pressures and moments are both plotted for the time of peak bending moment.

397 The bending moment data are captured quite well by the proposed solution in this case, whereas
398 the predicted soil pressures differ from the measured soil pressures. Although we show the measured
399 earth pressures for completeness, we focus our attention on bending moments for a number of reasons.
400 First, the strain gauges are considered to provide more reliable measurements than the tactile pressure
401 sensors (Dashti, personal communication 2017). Second, because of the aforementioned time difference
402 between predicted and measured soil pressures, a match would not necessarily be expected. Third,
403 bending moments are more important from a structural perspective.

404 Also plotted in Figs. 5 and 6 are solutions corresponding to the Seed and Whitman (S-W) method,
405 and in Fig. 5 for the Mononobe-Okabe (M-O) method. A friction angle of $\phi = 35°$ was utilized for these
406 solutions, as assumed by Hushmand et al. (2016). The M-O method does not produce a solution for the
407 Loma Prieta motion in Test 1 because the peak surface acceleration exceeded the M-O limiting value of
408 $PGA/g >= \tan(\phi)$, which is 0.7g (the measured PGA was 0.81g for the Loma Prieta motion in Test 1).

In the application of the S-W and M-O solutions, the earth pressure distribution was assumed to be triangular with the height of the resultant acting at h/H = 1/3. Seed and Whitman recommended placing the resultant at h/H = 0.6, but Mononobe and Matsuo (1929) found that (1/3H) is a more suitable resultant height for flexible walls. This is also consistent with recent observations by Wagner and Sitar (2017). Wall inertia is not included in the calculation of bending moment for the M-O and S-W solutions, which we believe is the most common approach adopted when computing bending moments arising from seismic earth pressures. The influence of wall inertia on these predictions is explored in the next section.

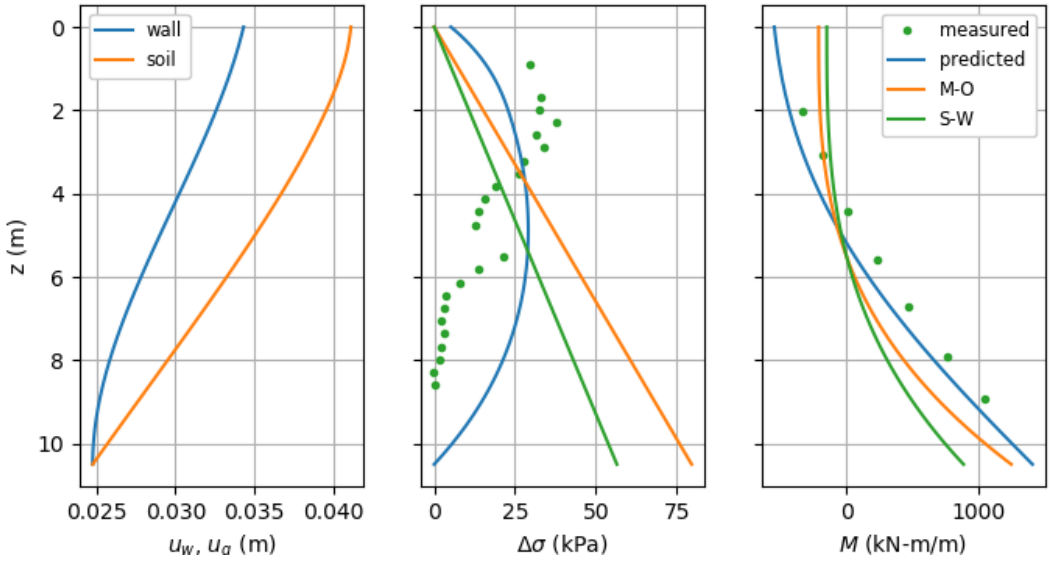

Figure 5. Predicted and measured response quantities for the Northridge-L motion applied to Test 2. Predictions include the method proposed in this study ("predicted"), the Mononobe-Okabe method ("M-O"), and by Seed and Whitman ("S-W"). The measured values of $\Delta\sigma$ were obtained by pressure cells, and values of M were evaluated from strain gauge data.

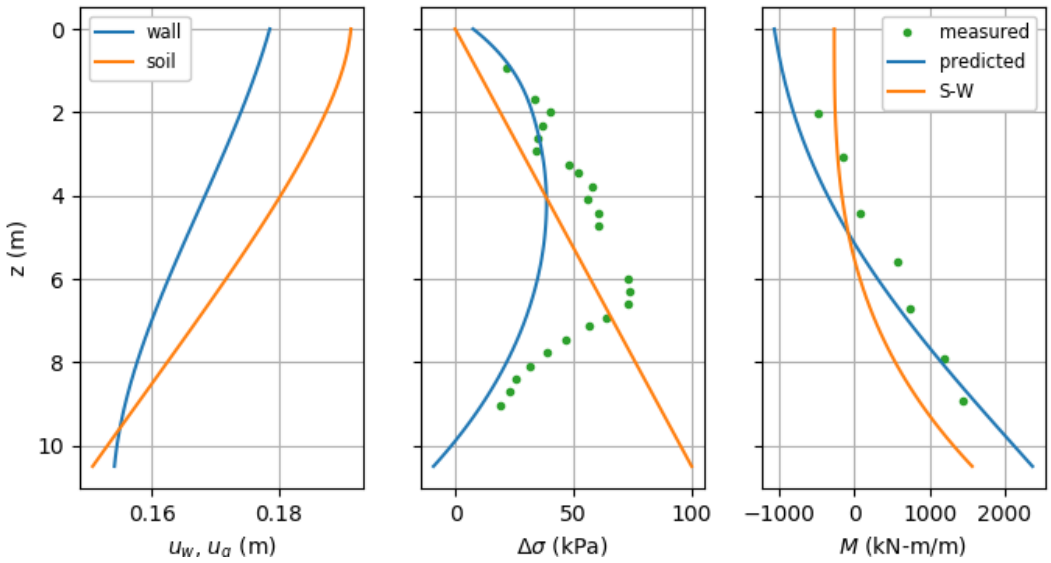

Figure 6. Predicted and measured response quantities for the Loma Prieta motion applied to Test 1. Predictions include the method proposed in this study ("predicted") and by Seed and Whitman ("S-W"). The Mononobe-Okabe method did not produce a solution for this motion.

The S-W and M-O solutions under-predict the measured bending moments in Fig. 5, and the S-W solution also under-predicts bending moments in Fig. 6. It is interesting that the S-W solution produces earth pressures in Fig. 6 that agree reasonably well with the measured peak pressures, but under-predicts bending moment. We attribute this to the lack of wall inertia in the S-W solution, and the resultant of the measured earth pressure distribution being higher than (h/H) = (1/3). The proposed solution predicts lower earth pressures, but higher bending moments compared with the S-W and M-O solutions. This is due to inertial interaction from the distributed mass along the wall and from lumped masses at the top and bottom of the wall, which are considered in the proposed solution, but not in the S-W and M-O solutions, as explored in more detail in the next section.

For the purpose of comparing measurements and predictions for all of the ground motions imposed on the model, we compute residuals defined as the natural log of the maximum measured bending moment minus the natural log of the maximum bending moment predicted at the same elevation.

Residuals are summarized in Table 2, and plotted in Fig. 7. For the proposed solution, the mean and standard deviation of the residuals are 0.11 and 0.34, respectively. For comparison, Fig. 7(b) plots residuals for the Mononbe-Okabe solution and Fig. 7(c) plots residuals for the Seed and Whitman (1973) solution. The mean and standard deviation for the M-O solution are computed only for the physically meaningful solutions (*PGA* < 0.7g), and are 0.29 and 0.32, respectively. The mean and standard deviation for the Seed and Whitman method in this case were 0.63 and 0.29, respectively. These positive means indicate under-prediction by approximately 26% (M-O) and 47% (S-W), whereas the proposed solution produces a much lower error (10%). The standard deviations of the residuals are similar for the three methods.

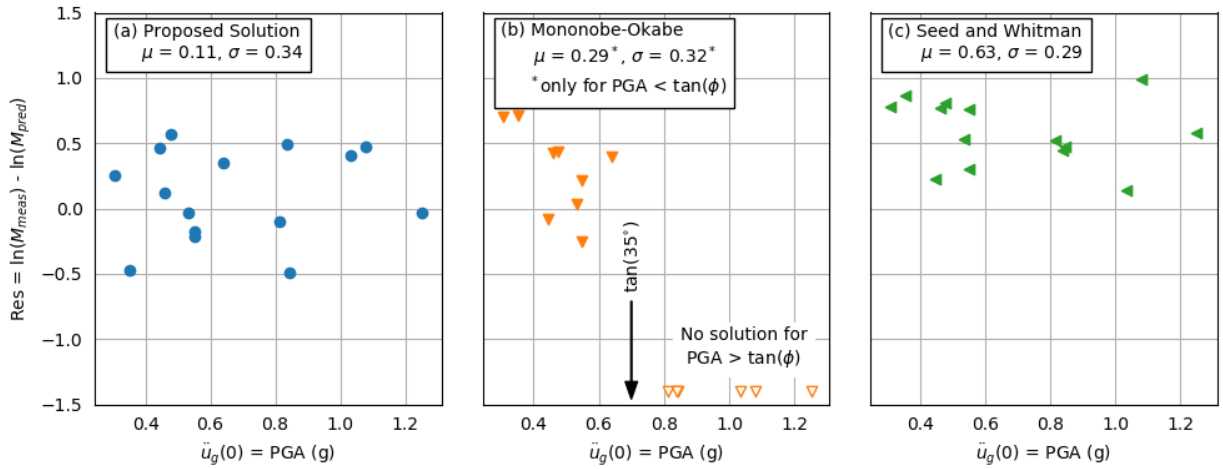

Figure 7. Residuals for the proposed solution, the Mononobe-Okabe method, and the Seed and Whitman method.

Table 2. Comparison of measured and predicted bending moments and residuals for experiment by Hushmand et al. (2016).

Test	Motion	PGA (g)	PGV (m/s)	PGD (m)	T_m (s)	M_{meas} (kN-m/m)	M_{pred} (kN-m/m)	$M_{M\text{-}O}$ (kN-m/m)	$M_{S\text{-}W}$ (kN-m/m)	Res_{pred}	$Res_{M\text{-}O}$[a]	$Res_{S\text{-}W}$
1	Izmit	0.53	0.54	0.09	0.49	965	993	936	565	-0.03	0.03	0.53
1	LomaPrieta	0.81	0.73	0.20	0.60	1452	1597	N/A	862	-0.09	-1.40	0.52
1	Northridge-H	0.84	1.05	0.31	0.84	1440	2357	N/A	895	-0.49	-1.40	0.48
1	Northridge-L	0.35	0.51	0.13	0.78	888	1422	435	374	-0.47	0.71	0.87
1	Northridge-M	0.55	0.73	0.24	0.83	1246	1491	1005	583	-0.18	0.22	0.76
2	Izmit	0.55	0.44	0.05	0.44	785	974	1005	583	-0.22	-0.25	0.30
2	LomaPrieta	1.25	0.85	0.20	0.50	2359	2443	N/A	1325	-0.04	-1.40	0.58
2	Northridge-H	1.08	0.74	0.23	0.63	3091	1922	N/A	1144	0.47	-1.40	0.99
2	Northridge-L	0.46	0.36	0.07	0.56	1049	929	687	487	0.12	0.42	0.77
2	Northridge-M	0.64	0.55	0.13	0.56	2318	1631	1565	678	0.35	0.39	1.23
4	Izmit	0.44	0.49	0.09	0.52	514	324	557	408	0.46	-0.08	0.23
4	LomaPrieta	1.03	0.73	0.18	0.60	1094	726	N/A	952	0.41	-1.40	0.14
4	Northridge-H	0.84	0.97	0.25	0.86	1204	735	N/A	772	0.49	-1.40	0.44
4	Northridge-L	0.31	0.49	0.11	0.87	616	476	306	282	0.26	0.70	0.78
4	Northridge-M	0.48	0.76	0.20	0.85	986	558	640	439	0.57	0.43	0.81

[a]Mononobe-Okabe procedure does not provide a solution for PGA > 0.7g for this problem.

Influence of Inertial Interaction

The distributed mass of the wall and lumped masses at the top and bottom of the wall were included in the predictions using the proposed solution, but not for the M-O and S-W solutions. This raises two questions: (*i*) what if inertia was added to the S-W and M-O solutions, and (*ii*) what if inertia was removed from the proposed solution? To answer the first question, bending moments for the M-O and S-W solutions were re-computed with consideration of inertial loads; the resulting residuals are plotted in Fig. 8. The acceleration was assumed to be equal to PGA when computing these forces, and half of the wall mass was lumped at the top and half at the bottom. As expected, the computed bending moments increase, which causes the residuals to decrease. The mean value of the residuals for the M-O and S-W methods now become negative, indicating over-prediction.

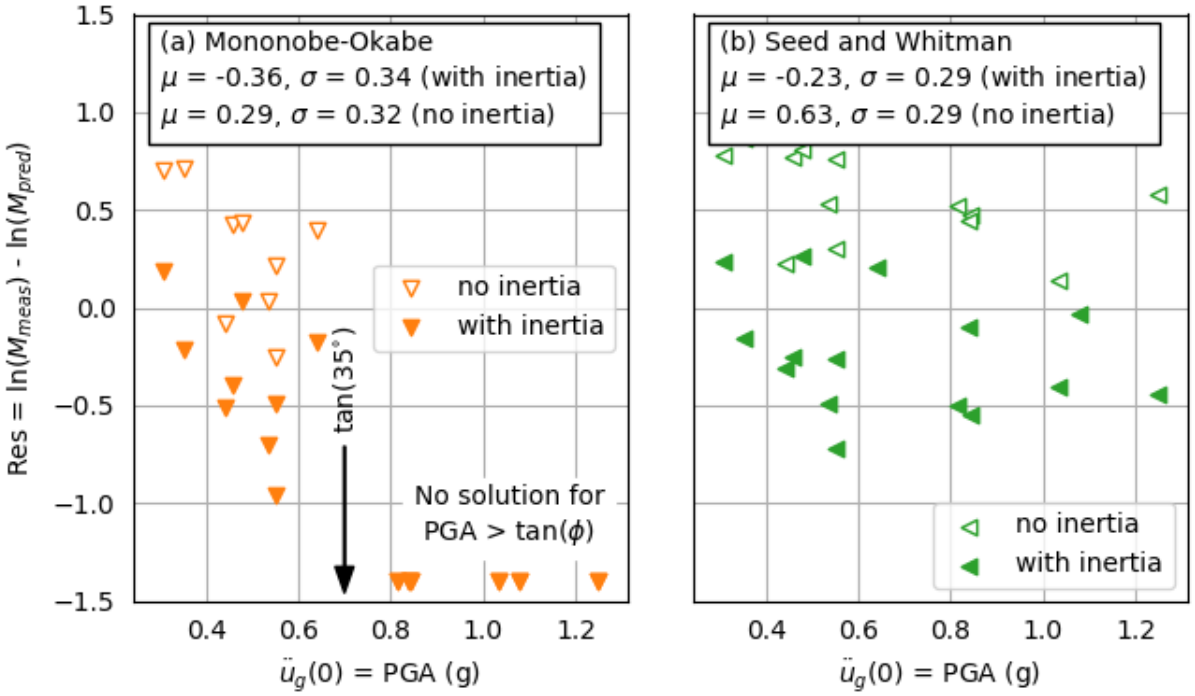

Figure 8. Residuals for (a) the Mononobe-Okabe method with and without wall inertia, and (b) the Seed and Whitman method with and without wall inertia. Values of μ and σ are computed for the cases with wall inertia.

To investigate the significance of inertial effects in the proposed solution, bending moment profiles were re-computed with the mass terms set to zero, which corresponds to a kinematic-only solution. Residuals for the solution without mass are plotted in Fig. 9 using solid symbols, along with residuals for the solution with mass plotted using open symbols. The mean of the residuals for the solution without mass is $\mu = 0.46$, indicating that excluding mass results in an under-prediction of bending moment. The differences in residuals with inertia and without inertia are more significant for the M-O and S-W procedures (differences in mean residuals of about 0.65-0.85, Fig. 8) than for the proposed solution (difference of 0.4, Fig. 9). This occurs because the earth pressure distribution in the proposed method is an outcome of the solution rather than a prescribed boundary condition. When wall inertia is added on top of the earth pressures computed using the M-O or S-W method, the wall displaces more in response to the inertial loading but the earth pressures remain the same.

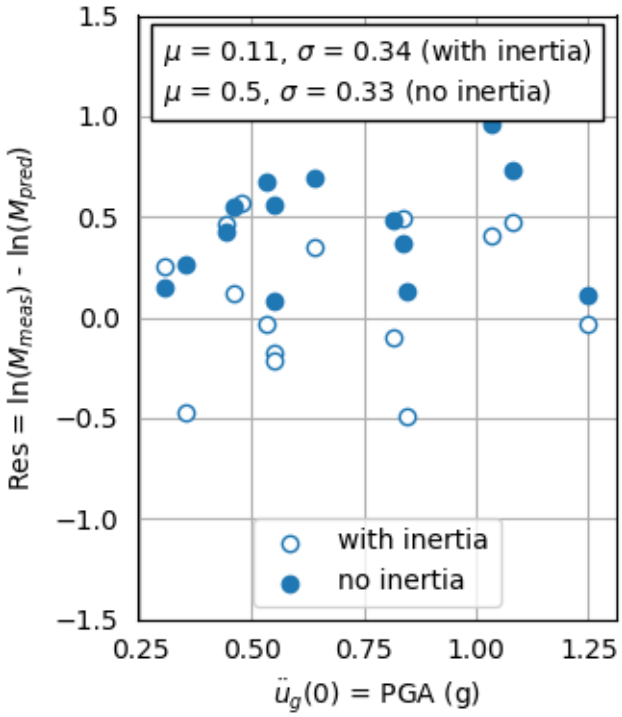

Figure 9. Residuals for proposed solution with and without wall inertia. Values of μ and σ are computed for the cases without wall inertia.

485 Distributions with depth of soil and wall displacement, earth pressure, and bending moment are
486 shown in Fig. 10 for Test 2 for the Northridge-L motion for cases with and without inertia. The bending
487 moments are larger for the simulation with inertia, but the mobilized earth pressure is smaller. The
488 reason for this behavior is that inertial loading tends to displace the wall away from the free-field soil,
489 which causes an increase in bending moment and a reduction in earth pressures. This is a fundamental
490 aspect of soil structure interaction that is captured by the proposed solution, but cannot be captured by
491 limit equilibrium methods such as M-O and S-W. Similar phasing differences between kinematic and
492 inertial demands were observed by Athanasopoulos-Zekkos et al. (2013).

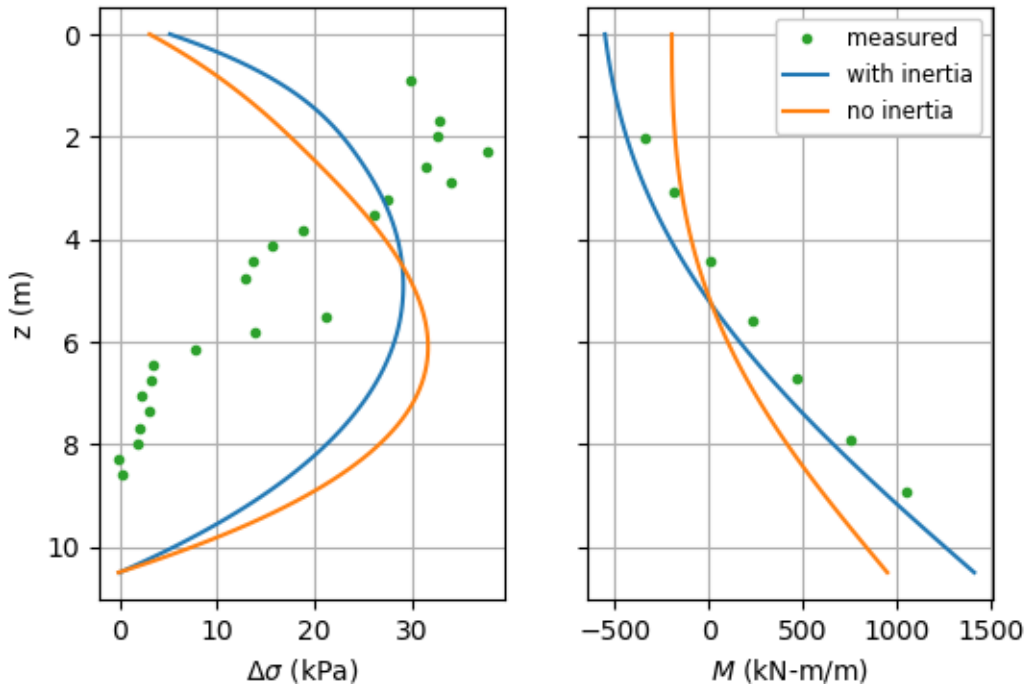

493

494 **Figure 10.** Distributions of soil and wall displacement, seismic earth pressure, and bending moment for
495 the Northridge-L motion for Test 2 for simulations with and without inertia loading.

Conclusions

A Winkler solution was formulated for the response of flexible retaining walls to vertical wave propagation through inhomogeneous soils. A closed-form exact solution to the governing differential equation of motion does not exist, so an approximate solution was formulated using the weak form of the equation. Soil-structure interaction is modeled using non-uniform Winkler stiffness intensity distributed along the wall, and impedance functions at the top and bottom of the wall. Mass distributed along the length of the wall and lumped at the top and bottom of the wall are included in the solution. The solution is first verified using a closed-form Winkler solution for homogeneous soil, then with a more robust continuum elastodynamic solution. Finally, the proposed solution is validated using measurements from a recent experimental study, and shown to produce more accurate predictions than the limit state procedures that are commonly utilized in practice.

Predictions from the proposed solution compare favorably with experimental data, but nevertheless exhibited differences between predicted and measured peak bending moment values. These differences arise, in part, from limitations of the proposed method, which include:

1. Soil inelasticity is modeled using the equivalent linear (EL) method, which is a common assumption made in ground response and soil-structure interaction analyses. However, the EL method is known to produce erroneous estimates of ground motion when shaking intensity becomes strong (e.g., Zalachoris and Rathje 2015; Kim et al. 2016). The EL method is not only used in estimating the distribution of free-field soil displacement along the height of the wall, but also in the Winkler stiffness intensity distributed along the wall height. It is unclear the extent to which this assumption introduces errors in the predictions.
2. Geometric nonlinearity may arise in the formation of gaps at the soil-wall interface (which might be more important for clayey backfills), but gapping is not modeled in the proposed solution.

3. The proposed solution utilizes the Winkler assumption, which is known not to faithfully model a continuum, but is useful when the Winkler stiffness intensity is carefully selected.

In addition to these limitations that may have influenced comparisons with experimental data, the proposed solution also does not consider: (1) coupling of soil and water response in saturated fill, including effects such as soil liquefaction and ground failure, pore pressures arising at the soil-wall interface, and propagation of p-waves through the fluid phase, and (2) nonlinear material behavior in the wall's structural elements. Limitations in the proposed method can be overcome using numerical analyses specifically formulated for a particular problem.

Structural components that are not explicitly modeled in the proposed solution are represented by lumped mass and stiffness terms. This modeling approach may be inadequate for cases where a structure attached to the top of the wall(s) or base slab exhibits a dynamic response that contributes additional inertial forces to the walls. This additional inertial interaction may contribute significantly to mobilized earth pressures, and can be modeled using techniques described by Stewart et al. (2012).

We advocate that the seismic response of retaining walls should be assessed using procedures that properly account for aspects of soil-structure interaction that strongly influence response. Limit state procedures, such as the Mononobe-Okabe method and Seed and Whitman method, that have been commonly utilized for nearly the past century, are not formulated to consider relative wall-soil displacement as a driver of seismic earth pressure. As a result, they do not account for important factors that influence relative displacements and the wall pressures they produce such as wall flexibility, soil inhomogeneity, and frequency content of the ground motion. Moreover, the M-O procedure does not provide a physically meaningful solution when the input acceleration becomes larger than a threshold value, which often occurs in high seismicity regions. The proposed solution, by contrast, considers wall

flexibility, soil inhomogeneity, and ground motion frequency content, which results in more accurate predictions.

Acknowledgments

This study benefitted from access to data from the experimental program described in Hushmand et al. (2016). Partial support for the second author was provided by Caltrans under contract number 65A0413.

Appendix. Derivation of Stiffness matrix, mass matrix, and force vector expressions.

To avoid disrupting the flow of the paper, derivations of the weak form of the governing differential equation, and the resulting stiffness matrices, mass matrices, and force vectors are presented in this appendix. The weak form of the governing differential equation is obtained by twice integrating by parts the first term on the left side of Eq. 16, resulting in Eq. 25.

$$EI\frac{\partial^3 u(z)}{\partial z^3}\Phi_j(z)\Big|_0^H - EI\frac{\partial^2 u(z)}{\partial z^2}\frac{\partial \Phi_j(z)}{\partial z^3}\Big|_0^H + EI\int_0^H \frac{\partial^2 u(z)}{\partial z^2}\frac{\partial^2 \Phi_j(z)}{\partial z^2}dz + \cdots$$
$$\cdots + k_{yH}^i\int_0^H f(z)u(z)\Phi_j(z)\,\mathrm{dz} - \rho_w t_w \omega^2\int_0^H u(z)\Phi_j(z)\,\mathrm{dz} = k_{yH}^i\int_0^H f(z)u_g(z)\Phi_j(z)\,\mathrm{dz} \quad (25)$$

Substituting Eq. 17 into Eq. 25 for *u(z)*, results in Eq. 26. Various terms in Eq. 26 have been assigned as either a stiffness matrix, $\mathbf{K}$, mass matrix, $\mathbf{M}$, or force vector, $\mathbf{F}$, and the c_i coefficients have been algebraically isolated in each expression.

$$\overbrace{EI\cdot\frac{\partial^3 \mathrm{u}(z)}{\partial z^3}\Phi_j(z)\Big|_0^H - EI\cdot\frac{\partial^2 u(z)}{\partial z^2}\frac{\partial\Phi_j(z)}{\partial z}\Big|_0^H}^{\mathbf{F^{reac}}} + c_i\cdot\overbrace{EI\int_0^H\frac{\partial^2\Phi_i(z)}{\partial z^2}\frac{\partial^2\Phi_j(z)}{\partial z^2}dz}^{\mathbf{K^a}} + \cdots$$
$$\cdots + c_i\cdot\underbrace{k_{yH}^i\int_0^H f(z)\Phi_i(z)\Phi_j(z)\,\mathrm{d}z}_{\mathbf{K^b}} - c_i\cdot\underbrace{\rho_w t_w\omega^2\int_0^H\Phi_i(z)\Phi_j(z)\,\mathrm{d}z}_{\mathbf{M^a}} = \underbrace{k_{yH}^i\int_0^H f(z)u_g(z)\Phi_j(z)\,\mathrm{d}z}_{\mathbf{F^a}} \tag{26}$$

555 The expression for $\mathbf{K^a}$ is provided by Eq. 27, and represents the traditional stiffness matrix for an Euler-
556 Bernoulli flexural plate.

$$K_{ij}^a = EI\int_0^H\Phi_i^{"}(z)\Phi_j^{"}(z)\,\mathrm{d}z = \frac{EI}{H^3}\begin{bmatrix}12 & 6H & -12 & 6H\\ 6H & 4H^2 & -6H & 2H^2\\ -12 & -6H & 12 & -6H\\ 6H & 2H^2 & -6H & 4H^2\end{bmatrix} \tag{27}$$

557 The expression for $\mathbf{K^b}$ was obtained using integration by parts and the general Leibniz rule for
558 differentiation of products of functions (e.g., Olver 2000), and is given by Eq. 28. Although this
559 expression is exact, its implementation may be susceptible to floating point errors. The integration was
560 performed here using numerical integration by the trapezoidal rule to avoid these errors.

$$K_{ij}^b = k_{yH}^i\int_0^H f(z)\,\Phi_i(z)\Phi_j(z)\,\mathrm{d}z = \sum_{a=0}^{6}\left\{\sum_{k=0}^{a}\left[\frac{a!}{k!(a-k)!}\Phi_i^{(a-k)}(z)\cdot\Phi_j^{(k)}(z)\right]\frac{-\left[b+(1-b)\frac{z}{H}\right]^{2n+a+1}}{(b-1)^{a+1}\prod_{m=1}^{a+1}(2n+m)}\Bigg|_{z=0}^{H}\right\} \tag{28}$$

561

562 The mass matrix $\boldsymbol{M^a}$ is given by Eq. 29, and represents the contribution of distributed mass along the
563 wall.

$$M_{ij}^a = \rho_w t_w\int_0^H\Phi_i(z)\Phi_j(z)\,\mathrm{d}z = \frac{\rho_w t_w}{420}\begin{bmatrix}156H & 22H^2 & 54H & -13H^2\\ 22H^2 & 4H^3 & 13H^2 & -3H^3\\ 54H & 13H^2 & 156H & -22H^2\\ -13H^2 & -3H^3 & -22H^2 & 4H^3\end{bmatrix} \tag{29}$$

564 The expression for the force vector $\mathbf{F^a}$ is given by Eq. 30. This expression is not integrable, and was
565 solved using numerical integration by the trapezoidal rule.

$$F_j^a = k_{yH}^i \int_0^H f(z) u_g(z) \Phi_j(z) dz \tag{30}$$

Having solved for the stiffness matrices, mass matrix, and force vector terms in Eq. 26, the remaining task is to solve for the first two terms that arise from integration by parts. Evaluating these terms over the limits results in a vector of shear and moment reaction forces at the top and base of the wall given by $\mathbf{F}^{\text{reac}} = EI \left\{ \frac{\partial^3 u(0)}{\partial z^3} \quad \frac{\partial^2 u(0)}{\partial z^2} \quad \frac{\partial^3 u(H)}{\partial z^3} \quad \frac{\partial^2 u(H)}{\partial z^2} \right\}^T$. These reaction forces are represented as a function of the nodal displacement coefficients, c_i, by creating stiffness matrices, a mass matrix, and a force vector representing the springs and lumped masses at the top and base of the wall.

The expression for $\mathbf{K}^{\mathbf{c}}$ represents the stiffness imposed on the wall by soil-structure interaction, and derived based on relative displacements between the wall and the soil either in the free-field (for an infinite length deposit), or at a position y_{ref} from the wall (for a finite-length deposit). When the base and roof diaphragms are rigid, $\mathbf{K} = \widehat{\mathbf{K}}$. However, in the case of flexible roof and base diaphragms, additional steps are required to compute the stiffness at the base. The approach adopted herein is to compute a uniform Winkler stiffness intensity for springs acting on the diaphragm that result in the rotational stiffness, $\widehat{K}_{xx,b}$, for a rigid wall. The resulting equivalent Winkler stiffness intensity is given by Eq. 31

$$k_z^i = \frac{24 \widehat{K}_{xx,b}}{B^3} \tag{31}$$

The rotational stiffness at the connection between the wall and base slab is then computed by imposing a unit rotation on the nodes at the ends of the base slab and solving for the bending moment, which results in Eq. 32, where $\beta_b = \sqrt[4]{k_z^i / 4EI_b}$, and EI_b is the flexural stiffness of the base slab.

$$K_{xx,b} = 2\beta_b^{\,2} EI_b \begin{Bmatrix} 0 & 1 & 0 & -1 \end{Bmatrix} \begin{bmatrix} 1 & 0 & 1 & 0 \\ -\beta_b & \beta_b & \beta_b & \beta_b \\ e^{-\beta_b B}\cos(\beta_b B) & e^{-\beta_b B}\sin(\beta_b B) & e^{\beta_b B}\cos(\beta_b B) & e^{\beta_b B}\sin(\beta_b B) \\ -\beta_b e^{-\beta_b B}\left[\cos(\beta_b B)+\sin(\beta_b B)\right] & \beta_b e^{-\beta_b B}\left[\cos(\beta_b B)-\sin(\beta_b B)\right] & \beta_b e^{\beta_b B}\left[\cos(\beta_b B)-\sin(\beta_b B)\right] & \beta_b e^{\beta_b B}\left[\cos(\beta_b B)+\sin(\beta_b B)\right] \end{bmatrix}^{-1} \begin{Bmatrix} 0 \\ 1 \\ 0 \\ 1 \end{Bmatrix} \quad (32)$$

583 Noting that $u_3 = u_g(0)$, $\theta_3 = 0$, $u_4 = u_g(H)$, and $\theta_4 = 0$, expressions for $\mathbf{K^c}$ and $\mathbf{F^c}$ are given by Eqs. 33 and

584 34.

$$\mathbf{K^c} = \begin{bmatrix} K_{y,t} & 0 & 0 & 0 \\ 0 & K_{xx,t} & 0 & 0 \\ 0 & 0 & K_{y,b} & 0 \\ 0 & 0 & 0 & K_{xx,b} \end{bmatrix} \quad (33)$$

$$\mathbf{F^c} = \begin{Bmatrix} K_{y,t} \cdot u_g(0) \\ 0 \\ K_{y,b} \cdot u_g(H) \\ 0 \end{Bmatrix} \quad (34)$$

585 The masses lumped at the top and bottom of the wall result in the mass matrix, $\mathbf{M^b}$ in Eq. 35.

$$\mathbf{M^b} = \begin{bmatrix} m_t & 0 & 0 & 0 \\ 0 & 0 & 0 & 0 \\ 0 & 0 & m_b & 0 \\ 0 & 0 & 0 & 0 \end{bmatrix} \quad (35)$$

586 Values of shear and moment at the top and bottom of the wall are then computed using Eq. 36.

$$\mathbf{F^{reac}} = \mathbf{K^c} - \omega^2 \mathbf{M^b c} - \mathbf{F^c} \quad (36)$$

587 Substituting Eq. 36 into 26 and collecting terms results in Eq. 37. Values of $\mathbf{c}$ are then solved by matrix

588 inversion.

$$\mathbf{c} = \left[\mathbf{K^a} + \mathbf{K^b} + \mathbf{K^c} - \omega^2 \mathbf{M^a} - \omega^2 \mathbf{M^b}\right]^{-1} \left\{\mathbf{F^a} + \mathbf{F^c}\right\} \quad (37)$$

589

590 **References**

591 Anoyatis, G., Di Laora, R., Mandolini, A., and Mylonakis, G. (2013). Kinematic response of single piles for
592 different boundary conditions: analytical solutions and normalization schemes. *Soil Dynamics and*
593 *Earthquake Engineering*, 44, 183-195.

Athanasopoulos-Zekkos, A., Vlachakis V.A., Athanasopoulos G.A. (2013). “Phasing issues in the seismic response of yielding, gravity-type earth retaining walls–Overview and results from a FEM study”, *Soil Dynamics and Earthquake Engineering*, 55, 59-70

Bielak, J., Loukakis, K., Hisada, Y., Yoshimura, C. (2003). "Domain Reduction Method for Three-Dimensional Earthquake Modeling in Localized Regions, Part I: Theory." *Bulletin of the Seismological Society of America*. 93(2). 817–824.

Borowicka, H. (1939). “Druckverteilung unter elastischen platten.” *Ingenieur Archiv*, 10(2), 113-125. doi: 10.1007/BF02084278

Brandenberg, S.J., Mylonakis, G., and Stewart, J.P. (2015) "Kinematic framework for evaluating seismic earth pressures on retaining walls." *J. Geotech. Geoenviron. Eng.*, 10.1061/(ASCE)GT.1943-5606.0001312, 04015031.

Brandenberg, S.J., Mylonakis, G., and Stewart, J.P. (2017). "Approximate solution for seismic earth pressures on rigid walls retaining inhomogeneous elastic soil." *Soil Dynamics and Earthquake Engineering*. 97, 486-477.

Brandenberg, S.J., and Durante, M. (2019). "Winkler solution for seismic earth pressures exerted on flexible walls by vertically inhomogeneous soil: Numerical implementation." DesignSafe-CI. https://doi.org/10.17603/ds2-2a8t-4v50.

Chen, W.F. (1975). "Limit analysis and soil plasticity. Developments in geotechnical engineering." Elsevier, Amsterdam, Netherlands.

Chen, W.F., and Liu, X.L. (1990). "*Limit analysis in soil mechanics*." Elsevier, Amsterdam, Netherlands.

Darendeli, M.B. (2001). "Development of a new family of normalized modulus reduction and material damping curves." *PhD thesis*, University of Texas, Austin, TX.

Durante, M.G., Brandenberg, S.J., Stewart, J.P., and Mylonakis, G. (2018). "Winkler stiffness intensity for flexible walls retaining inhomogeneous soil." *Geotechnical Earthquake Engineering and Soil Dynamics V: Numerical Modeling and Soil-Structure Interaction,* 473-482

Hashash, Y.M.A., Musgrove, M.I., Harmon, J.A., Groholski, D.R., Phillips, C.A., and Park, D., (2016). DEEPSOIL 6.1, User Manual.

Hushmand, A., Dashti, S., Davis, C., and Hushmand, B. (2016). "Seismic performance of underground reservoir structures: Insight from centrifuge modeling on the influence of structure stiffness." *J. Geotech. Geoenviron. Eng.,* 142(7).

Katsiveli, E. (2020) “Nonlinear dynamic analysis of shallow foundations”, *PhD thesis*, University of Bristol, U.K.

Kim, B, Hashash, Y.M.A., Stewart, J.P., Rathje, E.M., Harmon, J.A., Musgrove, M.I., Campbell, K.W., and Silva, W.J. (2016). “Relative differences between nonlinear and equivalent-linear 1D site response analyses," *Earthquake Spectra*, **32**, 1845-1865.

Kloukinas, P, Langousis, M., Mylonakis, G. (2012). “Simple Wave Solution for Seismic Earth Pressures on Gravity Walls”, *J. Geotech, Geoenviron. Eng.* ASCE, 138(12), 1514–1519

631 Lysmer, J. and Kuhlemeyer, R. L. (1969). “Finite dynamic model for infinite media. *J. Eng. Mech. Div.*, 95,
632 859-878.

633 McGuire, W., Gallagher, R.H., and Zieman, R.D. (2015). "*Matrix Structural Analysis: Second Edition*."
634 CreateSpace Independent Publishing Platform. 482 p.

635 Mikola, R.G., Candia, G., and Sitar, N. (2016). "Seismic earth pressures on retaining structures and
636 basement walls in cohesionless soils." *J. Geotech. Geoenviron. Eng.* 142(10).

637 Mononobe, N., and Matsuo, M. (1929). "On the determination of earth pressures during earthquakes."
638 *Proceedings of World Engineering Congress*, October 29 to November 7, Tokyo, Japan.

639 Mylonakis, G., Kloukinas, P., and Papantonopoulos, C. (2007). "An alternative to the Mononobe-Okabe
640 equations for seismic earth pressures." *Soil Dynamics and Earthquake Engineering*, 27, 957-969.

641 NCHRP (National Cooperative Highway Research Program). (2008). "Seismic analysis and design of
642 retaining walls, buried structures, slopes, and embankments." *Rep. 611*, D.G. Anderson, G.R. Martin,
643 I.P. Lam, and J.N. Wang, eds., National Academies, Washington D.C.

644 Okabe, S. (1924). "General theory on earth pressure and seismic stability of retaining wall and dam."
645 *Japanese Society of Civil Engineering*, 12(4), 34-41.

646 Olver, P.J. (2000). "*Applications of lie groups to differential equations*." Springer, 2nd ed. 517p.

647 Rovithis, E.N., Parashakis, H., and Mylonakis, G.E. (2011). “1D harmonic response of layered
648 inhomogeneous soil: Analytical investigation.” *Soil Dynamics and Earthquake Engineering*, 31, 879-
649 890.

650 Scott, R.F. (1981). *Foundation Analysis*, Prentice Hall.

651 Seed, H.B., and Whitman, R.V. (1970). "Design of earth retaining structures for dynamic loads." *ASCE*
652 *Specialty Conference on Lateral Stresses in the Ground and Design of Earth Retaining Structures*, 22-
653 24 June, N.Y., U.S.

654 Seyhan, E and JP Stewart (2014). “Semi-empirical nonlinear site amplification from NGA-West 2 data and
655 simulations," *Earthquake Spectra*, 30, 1241-1256.

656 Steedman, R.S., and Zeng, X. (1990). "The influence of phase on the calculation of pseudo-static earth
657 pressure on a retaining wall." *Geotechnique*, 40(1), 103-112.

658 Stewart, J.P., Crouse, C.B., Hutchinson, T.C., Lizundia, B., Naeim, F., and Ostadan, F. (2012). “Soil-
659 structure interaction for building structures.” Report No. 12-917-21, *National Institute of Standards*
660 *and Technology*, Gaithersburg, MD. 292 p.

661 Veletsos, A.S., and Younan, A.H. (1994). "Dynamic modeling and response of soil-wall systems." *J.*
662 *Geotech. Eng.*, 120(12), 2155-2179.

663 Wagner, N., and Sitar, N. (2016). "On seismic response of stiff and flexible retaining structures." *Soil*
664 *Dynamics and Earthquake Engineering* 91, 284-293.

665 Wood, J.H. (1973). "Earthquake induced soil pressures on structures." *PhD Thesis*, California Institute of
666 Technology, Pasadena, CA.

667 Younan, A.H., and Veletsos, A.S. (2000). "Dynamic response of flexible retaining walls." *Earthquake*
668 *Engineering and Structural Dynamics*, 29(9), 1815-1844.

669 Zalachoris, G., and Rathje, E.M. (2015). "Evaluation of one-dimensional site response techniques using
670 borehole arrays." *J. Geotech. Geoenviron. Eng.,* Paper 04015053.